Effect of the imaginary part of the refractive index on light scattering by spheres

GEORGE WANG, AMITABHA CHAKRABARTI, AND CHRISTOPHER M. SORENSEN*

Department of Physics, Kansas State University, 116 Cardwell Hall, Manhattan, Kansas 66506-2601, USA
*Corresponding author: sor@phys.ksu.edu

For spheres of arbitrary radius R and complex index of refraction $n + i\kappa$, we identify a new parameter that indicates when the imaginary part κ seriously affects the scattering by a sphere. The parameter is $\kappa k R$, where k is the wave vector magnitude, such that when $\kappa k R$ grows larger than one, the scattering is affected and, when $\kappa k R > 3$, the effects saturate. The effects are uncovered and demonstrated with Q-space analysis. The physical basis for $\kappa k R$ lies in the fact that it is the ratio of the radius to the optical skin depth.   © 2015 Optical Society of America

OCIS codes: (290.0290) Scattering; (290.4020) Mie theory; (290.5825) Scattering theory.

1. INTRODUCTION

Mie theory describes light scattering by spheres [1–4]. It allows calculation of the differential and total scattering cross sections for any given size or refractive index. With a steady increase in computational power, the feasibility of calculating light scattering for very large sizes has improved drastically. This opens the opportunity to empirically study the nature of scattering with systematic, wide-ranging changes in the governing parameters.

The purpose of this paper is to examine how the imaginary part of the index of refraction of spheres affects the way they scatter light. In particular, we study the angular functionality of the scattered intensity, which is directly proportional to the differential scattering cross section and the phase function [4]. In our study, we will use an unconventional method to display the angular scattering dependency, Q-space analysis [5]. This analysis is based on the use of the magnitude of the scattering wave vector q as the independent variable where q is

$$q = 2k \sin(\theta/2), \tag{1}$$

$k = 2\pi/\lambda$, λ is the wavelength of incoming light, and θ is the scattering angle. Q-space analysis involves plotting the scattered intensity versus q on a log-log format, instead of the convention of using linear θ. The method was first applied to Mie scattering from spheres to uncover patterns in the scattering that involved power laws [6,7]. Recently, we have applied it to describe how Mie scattering from spherical particles crosses over to Fraunhofer diffraction by a circular obstacle in the limit of large size [8].

2. METHODS

We will write the sphere's complex index of refraction relative to the medium as

$$m = n + i\kappa, \tag{2}$$

with the real part denoted by n and the imaginary part denoted by κ. An important parameter for our analysis is

$$\rho' = 2kR \left| \frac{m^2 - 1}{m^2 + 2} \right|, \tag{3}$$

where R is the radius of the sphere. Note that ρ' is a product of $2kR$ times the square root of the Lorentz–Lorenz term [9]. We have shown recently [9] that the Mie scattering curves (i.e., scattered intensity as a function of angle or q) show universal behavior for the same ρ', regardless of having different values of R, k, or m. It is similar to the phase shift parameter, ρ [9]. Additional detail about ρ' is given in the appendix. We will also, when needed, normalize the intensity curves by the Rayleigh cross-section, I(Rayleigh), where

$$I(\text{Rayleigh}) = k^4 R^6 \left| \frac{m^2 - 1}{m^2 + 2} \right|^2. \tag{4}$$

Data for the Mie scattering were obtained using Philip Laven's MiePlot v4.304 using the watts/sq m versus the scattering angle mode with default settings [10]. Incoming light was $\lambda = 650$ nm using the point source light setting, and the particle was monodisperse in a vacuum. The incident light was polarized perpendicular to the scattering plane defined by the incident and scattered directions. The scattering angle was varied with a 0.01° angular resolution. The size parameter kR and index of refraction were varied between data sets.

A program was written that calculated the scattered intensity in the exact forward direction, $I(0)$, of progressively increasing size parameters, which was then normalized by the Rayleigh scattering cross section I(Rayleigh). Graphs were generated using Mathematica version 8.0.

3. RESULTS

Figure 1 is a plot of $I(qR)/I(\text{Rayleigh})$ versus the dimensionless qR. Three different sets of curves are shown, with each set having different, relatively large size parameters kR and imaginary parts of the refractive index κ for each curve, but the constant within each set is the product of the two, κkR. Figure 1 shows that, as κ increases, its value on its own is not what determines the shape of the intensity plot, but rather the product of its value and the size parameter together, making a new parameter κkR. In each case, the curves each bear a very striking resemblance to the other two when they all share the same κkR. The three κkR values chosen demonstrate three different ranges of κ relative to kR: low ($\kappa kR < 0.3$), medium or crossover ($\kappa kR \simeq 1$), and high ($\kappa kR > 3$). The primary change observed is suppression of the ripple structure, which has an approximate frequency of $\delta(qR) \approx \pi$ [11] at large qR. We will henceforth call this rippleless, large qR region the "tail." Once κkR is in the high range, no noticeable changes occur, except for the tail's behavior (see below). Suppression of ripples with increasing κ has been described previously for the scattering efficiency [4].

Another important feature displayed in Fig. 1 is that, in all cases, the Rayleigh normalized scattering in the tail approaches a line described by $(9/4)(qR)^{-4}$ at $qR = 2kR$. This feature is elaborated below.

The Q-space patterns in Mie scattering, described previously for purely real refractive indices, hence $\kappa = 0$, are a set of power law functionalities between the scattered intensity and the scattering wave vector magnitude q or, more generally, the dimensionless qR [5–7]. Figure 2 demonstrates these functionalities. When the size parameter is $kR = 10$ (upper graph in Fig. 2), a forward scattering regime with slope zero; hence $I \sim (qR)^0$ occurs for $qR < 1$, followed by, with increasing qR, a Guinier regime near $qR \approx 1$, a rough $I \sim (qR)^{-2}$ for $1 < qR < \rho'$, and a rough $I \sim (qR)^{-4}$ for $\rho' < qR \leq 2kR$ (see Refs. [5–7] for a complete discussion of these trends). Large $\kappa kR = 10$ suppresses the ripples everywhere. When $kR = 100$ (middle graph in Fig. 2), the −2 power law has given over to $I \sim (qR)^{-3}$ followed by a plateau with an approximately zero slope. This −3 slope regime is the onset of the crossover of three-dimensional spherical particle Mie scattering to two-dimensional circular aperture diffraction for large particles, as described recently [8]. For this size parameter, the large $\kappa kR = 10$ suppresses only the ripples that are not involved in the two-dimensional circular aperture diffraction. After the plateau, the −4 regime still occurs for $\kappa kR = 0$ and is trending to that for $\kappa kR = 10$ in the tail region. This behavior is
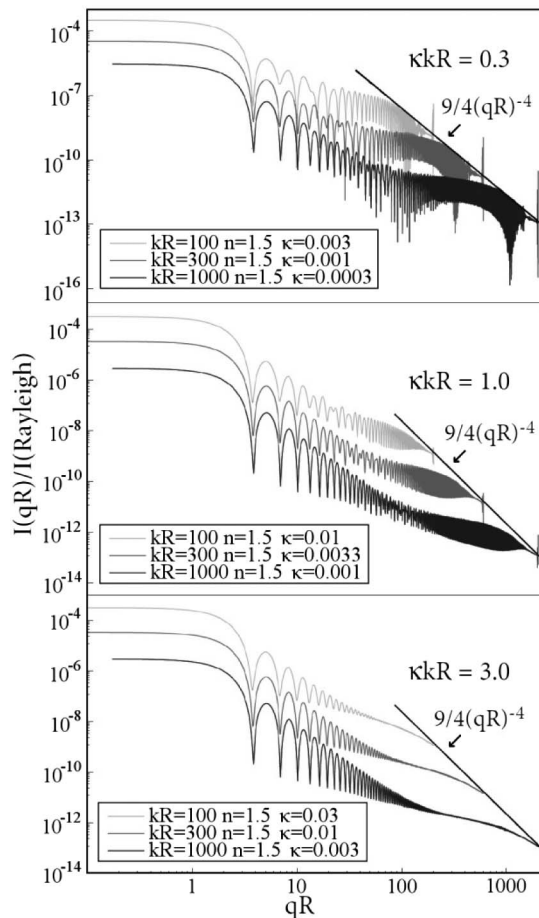
Fig. 1. Scattered intensity normalized by the Rayleigh cross section plotted versus qR grouped into three different values of κkR. Within each κkR group, there are three different size parameters.
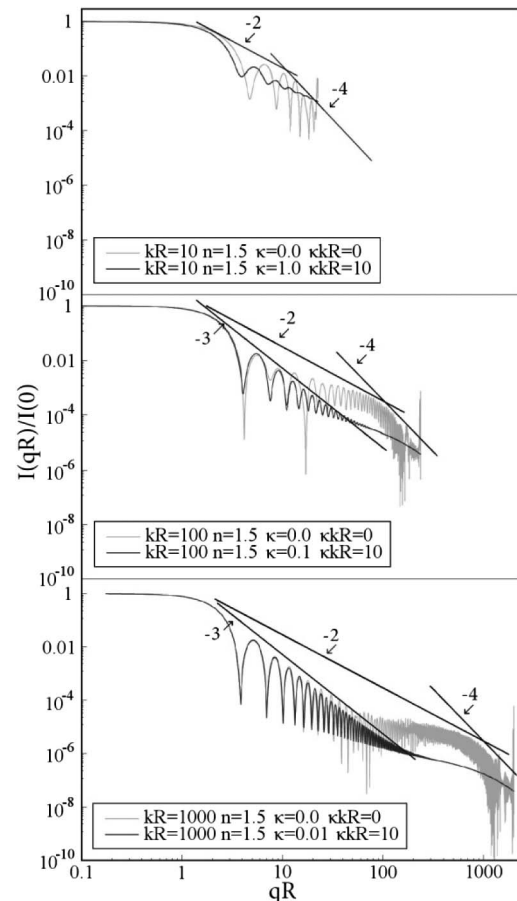
Fig. 2. Intensity plots of a high, $\kappa kR = 10$ curve compared with a curve with no κ. Initial intensity is normalized to unity and plotted versus qR.

more pronounced as kR increases, for example when $kR = 1000$ as shown in Fig. 2, bottom graph.

Figure 3 shows that, at large size parameters and κkR, in this case $kR = 1000$ and $\kappa kR = 10$, ripples in the intensity plot lie almost exactly on top of the circular aperture diffraction as described by [12]:
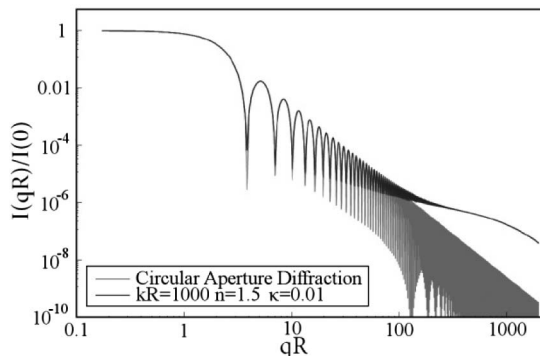
$$I(qR) = \left(\frac{2J_1(qR)}{qR}\right)^2. \tag{5}$$

In Eq. (5), $J_1(x)$ is the first Bessel function. This overlap continues up until the curve begins to transition into the tail region and, as long as it lies on top of the circular aperture diffraction, its envelope maintains a –3 power law. This is true for any intensity plot in the high κkR range with large kR. As the size parameter decreases, the forward scattering region of curves with high κkR starts to shift away gradually from circular aperture diffraction; however, they continue to maintain a very close resemblance. For $kR = 1000$, the transition into the tail region seems to occur mostly in the $qR = 70$ to $qR = 110$ range (Fig. 3). However, while qR_{max} is directly proportional to kR, when systematically reducing kR, there does not appear to be a linear relationship between the kR and the qR ranges where the transition occurs.
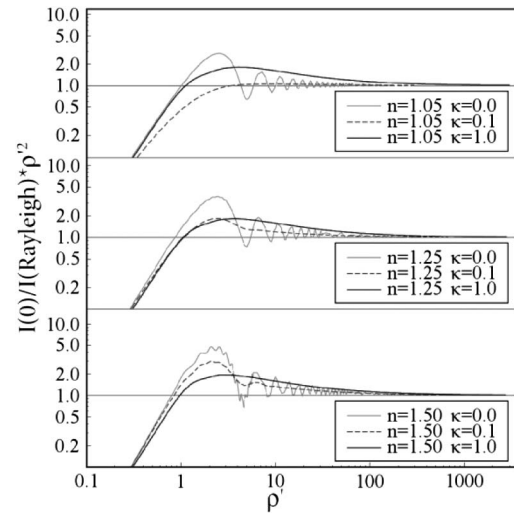
Figure 4 examines the behavior of Rayleigh normalized forward scattering intensities scaled by ρ'^2 and plotted against ρ'. As the size parameter increases ($kR = 0.1$ to $kR = 2000$), ρ' increases for a given refractive index; see Eq. (3). Now a different ripple structure than that portrayed in Figs. 1 and 2 is seen, but again the ripple is suppressed as κ increases. However, a hump near $\rho' \approx 2$ persists. Finally, the curves approach unity at large ρ' to imply that in this limit $I(0) = I(\text{Rayleigh})/\rho'^2 = k^2 R^4 / 4$ [9].

After Rayleigh normalization, patterns can be observed in the behavior of the tail as well (Fig. 5). The form that the tail takes depends on the ratio $\rho'/kR = 2|(m^2 - 1)/(m^2 + 2)|$. A low ρ'/kR ratio causes the tail to tend toward a –4 power law, while a high ρ'/kR ratio causes the tail to tend toward a plateau region. This occurs because, as the refractive index varies, the curves move up and down, but the end point at $qR_{max} = 2kR$ stays fixed on the $(9/4)(qR)^{-4}$ line.

Figure 6 explores the asymptotic approach toward the $(9/4)(qR)^{-4}$ line. Here the ρ' value for the curves was kept constant, and their Rayleigh normalized initial intensities are


Fig. 4. Rayleigh normalized forward scattering intensities multiplied by ρ'^2 plotted versus ρ' grouped into three different values of the real index of refraction n. Within each n group there are three different imaginary indices of refraction κ.
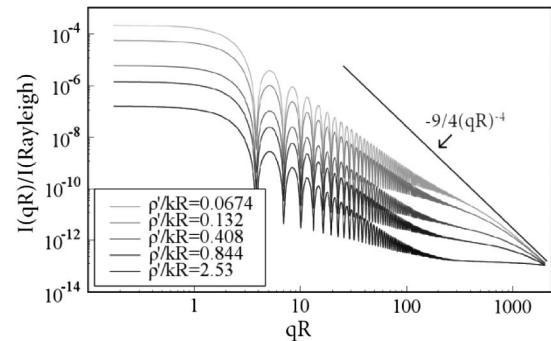
Fig. 5. Rayleigh normalized scattered intensity of various high κkR range ($\kappa kR > 3$) curves with different tail behaviors. The $(9/4)(qR)^{-4}$ line is shown.

Fig. 3. Comparison between circular aperture diffraction and Mie scattering for $\kappa kR = 10$.
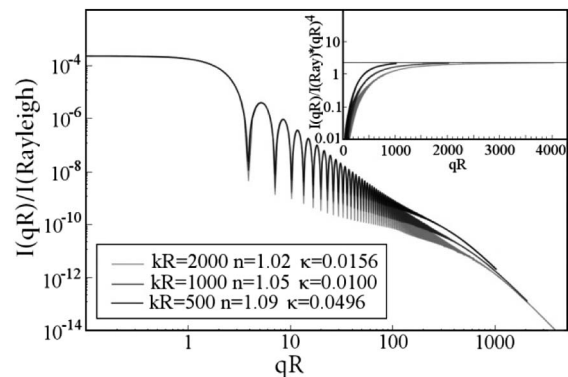
Fig. 6. Rayleigh normalized scattered intensity with constant $\rho' = 67.4$ plotted versus qR. The inset takes the intensity and scales it by $(qR)^4$ and is plotted versus linear qR. The 9/4 line is shown in the inset.
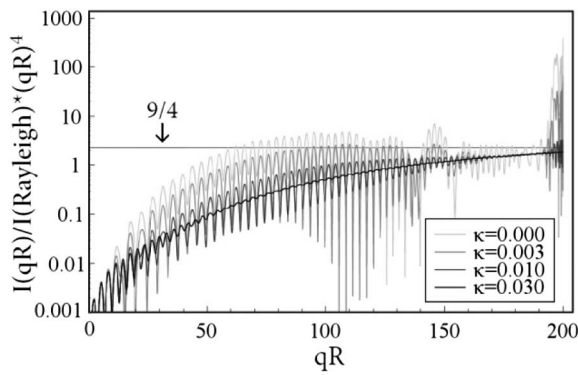
Fig. 7. Scattered intensity plots of increasing κ and constant $kR = 100$ and $n = 1.50$; Rayleigh is normalized, scaled by $(qR)^4$, and plotted versus qR to show the behavior of the tail.

the same. The curves have low enough ρ'/kR ratios that their tails exhibit a –4 power law, though they end at different points on the $(9/4)(qR)^{-4}$ line because of varying kR values. The inset magnifies the behavior of the tails and clearly shows that they approach the $(9/4)(qR)^{-4}$ line.

The results in Fig. 6 are when κkR is large; hence the tails of all the curves are smooth. Figure 7 takes a closer look at how the tail behaves as κ is slowly introduced. As κ transitions into the high κkR range, it seems to be geometrically averaging the ripples in the tail. This is especially apparent in the glory.

4. CONCLUSION AND DISCUSSION

We have identified a new parameter that indicates when the imaginary part of the refractive index κ seriously affects scattering by a sphere, the parameter κkR. We say "seriously" because κ is obviously involved in m which, in turn, is involved in the Lorentz-Lorenz term. When $\kappa kR < 1$, κ has little effect, but as κkR becomes comparable to one, the effects of κ are greater. Finally, when $\kappa kR > 3$, the effects of κ saturate and no further evolution with increasing κ occurs. To the best of our knowledge, there is no similar parameter or study of this kind in the literature.

The κkR parameter is related to the optical skin depth in the spheres. The skin depth (δ) is the $1/e$ depth that incoming light penetrates into an object and is related to the imaginary index by [12]:

$$\delta = \frac{\lambda_0}{2\pi\kappa}, \tag{6}$$

where λ_0 is the wavelength in a vacuum. Given this, the relative size of the skin depth to the sphere radius is

$$\frac{\delta}{R} = \frac{1}{\kappa kR}. \tag{7}$$

Thus, when two spheres share a common κkR, the ratio between their skin depth and radius is the same. What this means is that, when κkR is very small, δ is much larger than R, and the sphere is illuminated by the incident field unaffected by finite κ. δ is equal to R when $\kappa kR = 1$ and, hence, the effects of finite κ become important. Once $\kappa kR > 3$, δ is equal to or less than a third of R and, apparently, only the front "cap" of the particle

facing the incident light is responsible for the scattering. Moreover, our results imply that further thinning of this front cap has little effect on the scattering. However, what does remain at large κkR, hence small δ/R, is the fact that the sphere is now a two-dimensional obstacle with concomitant two-dimensional circular aperture diffraction.

We remark that our conclusions regarding κkR values were determined mostly for a real index of $n = 1.50$. In actuality, there is a small variation with the real index as well, but not enough to alter our conclusions above.

We can offer a tentative explanation for the loss of the ripples in the tail (non-two-dimensional diffraction) regime. Consider that light scattering is most fundamentally wave scattering, wave scattering is diffraction, diffraction is Fourier transformation. Fourier transformation of sharp boundaries causes ripples. When κkR becomes large, and the skin depth with its smooth, exponential decay begins to dominate the scattering, we expect the Fourier transformation aspect of light scattering to lose the ripples. On the other hand, the remaining front cap still has a sharp leading edge to cause the ripples in the two-dimensional circular aperture diffraction pattern.

We also can speculate that the glory and rainbows disappear because both require the back side of the sphere for their occurrence. This backside grows dark when κkR approaches unity.

Our biggest enigma, which we have not solved, is the $9/4(qR)^{-4}$ line. The –4 power law is a remnant of the $\rho' \to 0$ limit for spherical particle scattering, the Rayleigh-Debye-Gans limit, which is also the square of the Fourier transform of the sphere. We have discussed with some detail in our previous work the persistence of this functionality for spheres of arbitrary size and refractive index [5–9]. Moreover, we have presented arguments that, when the refractive index is completely real ($\kappa = 0$), the –4 power law is a consequence of the surface caps on the polar ends of the sphere as defined by the wave vector $\vec{q}$ acting as the polar axis [13]. Thus, a thinning cap due to finite κ causing –4 power law is consistent with this previous conclusion. The enigma is that the coefficient of the power law is 9/4 rather than 9 found for the RDG envelope.

The purpose of this paper is to explore theoretically the effects of the imaginary part of the refractive index on the scattering properties of spheres in the context of the Q-space analysis. New patterns of scattering behavior have been uncovered that will help us formulate a complete physical description of scattering based on this novel analysis. However, it is worth asking where the effects described here might appear in the physical world. Examples of small particles include soot compressed by atmospheric effects [14], which can have important effects for the global radiation budget, and metallic particles from nano to micro of gold [15], for example, which are at the forefront of new technologies. Many micron-sized solid particles occurring in nature are typically not spheres. However, the results here which are valid for spheres still should have some semi-quantitative bearing on such irregularly shaped particles since the concept of optical skin depth is independent of shape. Thus, for example, a 10 micron feldspar particle with a refractive index $m = 1.59 - i9 \times 10^{-3}$ [16] would have a $\kappa kR \simeq 1$. For this particle, given the results above,

one would expect the scattering to be dominated by diffraction with no interference ripples in the large qR regime. We also would like to point out that attenuation of the ripples and bending of the tail region might be useful for measurement of the imaginary part of the refractive index of a particle, although the former also is affected by particle polydispersity.

Finally, we remark that these new patterns described above would be very difficult to see and describe with the conventional log intensity versus the linear angle plotting method. Q-space analysis has allowed these patterns to be exposed.

APPENDIX A

The parameter $\rho' = 2kR[(m^2 - 1)/(m^2 + 2)]$ has a superior ability to organize patterns [5–7] in light scattering from uniform spheres of arbitrary size and refractive index than the well-known phase shift parameter $\rho = 2kR(m - 1)$ [2–4]. The new parameter also is more capable of describing the transition from simple wave diffraction (the Rayleigh-Debye-Gans limit) to the complete electromagnetic description of spherical particle light scattering. A complete description of ρ' has been submitted for publication [9].

REFERENCES

1. G. Mie, "Beiträge zur Optik trüber Medien speziell kolloidaler Metallösungen," Ann. Phys. **330**, 377–445 (1908).
2. H. C. van de Hulst, *Light Scattering by Small Particles* (Dover, 1981).
3. C. F. Bohren and D. R. Huffman, *Absorption and Scattering of Light by Small Particles* (Wiley, 1983).
4. M. I. Mishchenko, L. D. Travis, and A. A. Lacis, *Scattering, Absorption and Emission of Light by Small Particles* (Cambridge University, 2002).
5. C. M. Sorensen, "Q-space analysis of scattering by particles: a review," J. Quant. Spectrosc. Radiat. Transfer **131**, 3–12 (2013).
6. C. M. Sorensen and D. J. Fischbach, "Patterns in Mie scattering," Opt. Commun. **173**, 145–153 (2000).
7. M. J. Berg, C. M. Sorensen, and A. Chakrabarti, "Patterns in Mie scattering: evolution when normalized by the Rayleigh cross section," Appl. Opt. **44**, 7487–7493 (2005).
8. W. R. Heinson, A. Chakrabarti, and C. M. Sorensen, "Crossover from spherical particle Mie scattering to circular aperture diffraction," J. Opt. Soc. Am. A **31**, 2362–2364 (2014).
9. W. R. Heinson, A. Chakrabarti, and C. M. Sorensen, "A new parameter to describe the transition of light scattering from the Rayleigh-Debye-Gans limit," J. Opt. Soc. Am. A, submitted.
10. P. Levin, "Simulation of rainbows, coronas, and glories by use of Mie theory," Appl. Opt. **42**, 436–444 (2003).
11. C. M. Sorensen and D. Shi, "Patterns in the ripple structure in Mie scattering," J. Opt. Soc. Am. **19**, 122–125 (2002).
12. E. Hecht, *Optics*, 2nd ed. (Addison-Wesley, 1987).
13. M. J. Berg, C. M. Sorensen, and A. Chakrabarti, "Explanation of the patterns in Mie theory," J. Quant. Spectrosc. Radiat. Transfer **111**, 782–794 (2010).
14. X. Ma, C. D. Zangmeister, J. Gigault, G. W. Mulholland, and M. R. Zachariah, "Soot aggregate restructuring during water processing," J. Aerosol Sci. **66**, 209–219 (2013).
15. N. Pazos-Perez, F. J. Garcia de Arbajo, A. Fry, and R. A. Alvarez-Puebla, "From nano to micro: synthesis and optical properties of homogeneous spherical gold particles and their superlattices," Langmuir **28**, 8909–8914 (2012).
16. K. Kandler, N. Benker, U. Bundke, E. Cuevas, M. Ebert, P. Knippertz, S. Rodríguez, L. Schütz, and S. Weinbruch, "Chemical composition and complex refractive index of Saharan Mineral Dust at Izaña, Tenerife (Spain) derived by electron microscopy," Atmos. Environ. **41**, 8058–8074 (2007).